A novel P-block single metal-site Tin-Nitrogen-doped Carbon (Sn-N-C) Fuel Cell Cathode Catalyst for the Oxygen Reduction Reaction (ORR)

Fang Luo[1], Aaron Roy[2], Luca Silvioli[3,4], David A. Cullen[5], Andrea Zitolo[6], Moulay Tahar Sougrati[2], Ismail Can Oguz[2], Tzonka Mineva[2], Detre Teschner[7,8], Stephan Wagner[9], Ju Wen[1], Fabio Dionigi[1], Ulrike I. Kramm[9], Jan Rossmeisl[3*], Frédéric Jaouen[2*] and Peter Strasser[1*]

[1]*Department of Chemistry, The Electrochemical Energy, Catalysis and Material Science Laboratory, Chemical Engineering Division, Technical University Berlin, Straße des 17. Juni 124, 10623 Berlin, Germany.*

[2] *ICGM, Univ. Montpellier, CNRS, ENSCM, Montpellier, France.*

[3]*Nano-Science Center, Department of Chemistry, University Copenhagen, Universitetsparken 5, 2100 Copenhagen, Denmark.*

[4]*Seaborg Technologies, Titangade 11, 2200 Copenhagen, Denmark.*

[5]*Center for Nanophase Materials Sciences, Oak Ridge National Laboratory, Oak Ridge, TN 37831, UAS.*

[6]*Synchrotron SOLEIL, L'orme des Merisiers, BP 48 Saint Aubin, 91192 Gif-sur-Yvette, France.*

[7]*The Fritz-Haber-Institute der Max-Planck-Gesellschaft, Inorganic Chemistry-Electronic Structure Group, Berlin 14195, Germany.*

[8]*Department of Heterogeneous Reaction, Max-Planck-Institute for Chemical Energy Conversion, 45470 Mülheim an der Ruhr, 14195 Berlin, Germany.*

[9]*Department of Chemistry and Department of Materials and Earth Sciences, Graduate School of Excellence Energy Science and Engineering, Technical University Darmstadt, Otto-Berndt-Str. 3, 64287 Darmstadt, Germany.*

*To whom correspondence should be addressed:

*e-mail: pstrasser@tu-berlin.de; frederic.jaouen@umontpellier.fr; jan.rossmeisl@chem.ku.dk

Abstract

This contribution reports the discovery and analysis of the first PGM-free, p-block Sn-based single metal and nitrogen-doped carbon (MNC) catalysts for the electroreduction of molecular oxygen (ORR) in acidic conditions at fuel cell cathodes. The prepared SnNC catalysts meet and exceed state of art FeNC catalysts in terms of intrinsic catalytic turn over frequency (TOF) and hydrogen-air fuel cell power density. The SnNC-NH$_3$ catalysts displayed a 40-50% higher current density than FeNC-NH$_3$ at cell voltages below 0.7 V. Added benefits include a high favorable selectivity for the 4-electron reduction pathway and a Fenton-inactive character of Sn.

A range of analytical techniques, combined with DFT calculations indicate that stannic Sn(IV)-Nx single metal sites with moderate oxygen chemisorption properties and low pyridinic N coordination numbers act as catalytic active moieties. The superior PEMFC performance of SnNC cathode catalysts under realistic, hydrogen-air fuel cell conditions, particularly after NH$_3$ activation treatment, makes them a promising replacement of today's state-of-art Fe-based catalysts.

Growing concerns over fossil energy and the environment are incentives to develop new energy technologies. Low-temperature hydrogen/air proton-exchange membrane fuel cell (PEMFC) is one such technology, converting hydrogen into electrical energy[1, 2]. For catalyzing the oxygen reduction reaction (ORR) and hydrogen oxidation reaction at the electrodes, PEMFCs rely however on precious, in particular platinum-based catalysts[3, 4], a scarce and expensive metal. Research to replace precious group metals (PGMs) has led to a class of bio-inspired catalysts, labelled MNC, that involve non-precious 3d transition metal cations stabilized by nitrogen atoms (Metal-N_x moieties), themselves incorporated in conductive carbon matrices. Fe, Co and Mn are hitherto the only three metals that result in ORR-active Metal-N_x moieties in acidic reaction environments[5, 6, 7, 8, 9, 10]. While the number and utilization of such moieties embedded in carbon are being improved[9], the fundamental nature of such sites is not so new. Indeed, the large body of experimental research on pyrolyzed FeNC and CoNC materials identifies Metal-N_4 motifs as the most active sites for catalyzing ORR in acid[11, 12, 13]. Such sites are akin to square-planar Metal-N_4 sites in Fe or Co macrocycles, identified in 1964 to be ORR active [14]

Here, we report the discovery of the first p-block single metal site catalyst, SnNC, exhibiting catalytic ORR reactivities in acidic environments that meet and exceed all state-of-art PGM-free catalyst concepts, while adding important benefits in terms of catalyst stability. The catalytically active single-metal SnN_x moieties embedded in the surface of the SnNC catalyst were characterized by high-resolution scanning transmission electron microscopy (STEM) coupled with electron energy loss spectroscopy (EELS), extended X-ray absorption fine structure (EXAFS), X-ray photoelectron spectroscopy (XPS) and ^{119}Sn Mössbauer spectroscopy, complemented by Density Function Theory (DFT) calculations. The vast majority of Sn atoms are atomically dispersed and in close association with nitrogen atoms, while the average coordination numbers for Sn in the first coordination sphere are 3.9 in-plane (nitrogen and/or carbon atoms) and 1.0 above the plane (oxygen ligand). Both stannous and stannic species are present, the latter assigned mainly to surface $Sn(IV)N_x$ moieties. The average ORR turnover frequency (TOF) of the SnN_x sites meets that of the decade-long state-of-art FeN_x sites, yet ranges significantly higher than that of CoN_x sites. The fuel cell device performance of the new SnNC catalysts in real hydrogen PEMFCs exceeded those of an otherwise similarly prepared FeNC reference catalyst. The theoretical study reveals that p-block SnNx moieties do not follow, i.e. break the usual linear relationships between the chemisorption strength of adsorbed reactive oxygen intermediates[15, 16,

[17, 18], in sharp contrast to conventional d-block M-Nx moieties (M=Fe, Co, Ni, Cu). This sets the current SnNC catalyst apart from all previously described d-block catalysts and appears to be responsible for the observed high chemical selectivity to full O_2 reduction of SnN_x active sites.

Catalyst synthesis and the local chemical environment of the active sites

The synthesis of SnNC catalysts involved aniline polymerization, pyrolysis of polyaniline/metal precursor mixture, followed by multiple acid leaching steps (details in Supplementary Information). Similar preparation routes were used to prepare FeNC catalysts comprising atomically dispersed FeN_x sites[6, 9, 12], and such a FeNC material was used here as a benchmark. With cobalt however, the aniline polymerization approach leads to crystalline cobalt sulfide (not shown). For this reason, the sacrificial ZIF-8 approach was used for preparing another benchmark CoNC catalyst, exclusively comprising CoN_x moieties (details in Supplementary Information)[13]. The morphology and crystalline character of the SnNC, FeNC and CoNC catalysts were characterized first using TEM and X-ray diffraction (XRD). No peaks related to metal-based crystallographic structures are seen in the XRD patterns and no metal-rich particles are seen in TEM micrographs (**Figure S1**). Probing the electronic molecular environment of Fe centers in the reference FeNC, ^{57}Fe Mössbauer spectroscopy revealed two doublets assigned to FeN_4 moieties of different oxidation and spin states[19, 20] (**Figure S2**). Further analyses addressed the chemical compositions at surface and bulk of all catalysts (**Tables S1-S2**). The nitrogen content was similar among the catalysts at 6-6.5 at %, while the atomic content of Sn in SnNC was, as expected, about half of that of Fe in FeNC (0.4 and 0.9 at%, respectively, **Table S1**), given the difference in atomic weights and similar metal contents by weight (wt%). Narrow-scan Sn 3d photoemission spectra confirmed the possible coexistence of Sn(II) and Sn(IV) species in SnNC (**Figure 1a**), while X-ray absorption spectroscopy (XAS) at the Fe $L_{3,2}$ edge revealed the presence of Fe(II) and Fe(III) in FeNC (**Figure S3a**). The lack of spectroscopic fingerprints of zero-valent Sn agreed with the absence of metal cluster or particles in the TEM images. High resolution N 1s spectra were quite similar in SnNC and FeNC, with sp^2 -hybridized N in BE-range 1 (Imine/pyridinic/triazinic) and N in BE-range 3 (isolated graphitic N, hydrogenated/protonated N such as pyrrolic or protonated pyridinic) as the dominant chemical species (**Figure 1b**, **Figure S3b** and **Table S3**). To obtain insights in the local chemical environments, we performed aberration-corrected STEM and EELS that recently revealed the close proximity of N atoms around atomically-dispersed Fe atoms in

another FeNC catalyst[12]. STEM images of SnNC catalysts revealed a carbon matrix with randomly-oriented nanometric graphite crystallites (**Figure 1c**, **Figure S4a**). They also evidenced the random distribution of atomically dispersed Sn atoms (**Figure 1d-f**, **Figure S4b-d**). Direct evidence for the co-location of Sn and N atoms was demonstrated by EELS (**Figure 1f-g**), providing strong evidence for the coordination of Sn by nitrogen atoms in the $Sn-N_x$ moieties. The N/Sn ratio could however not be quantified by STEM/EELS, as this resulted in the displacement of Sn atoms under electronic beam. This contrasts with FeN_x sites in Fe-N-C, indicating weaker binding of Sn cations to the N-C matrix. To obtain additional atomic-scale information, we resorted to X-ray absorption near edge structure (XANES) and EXAFS spectroscopies.
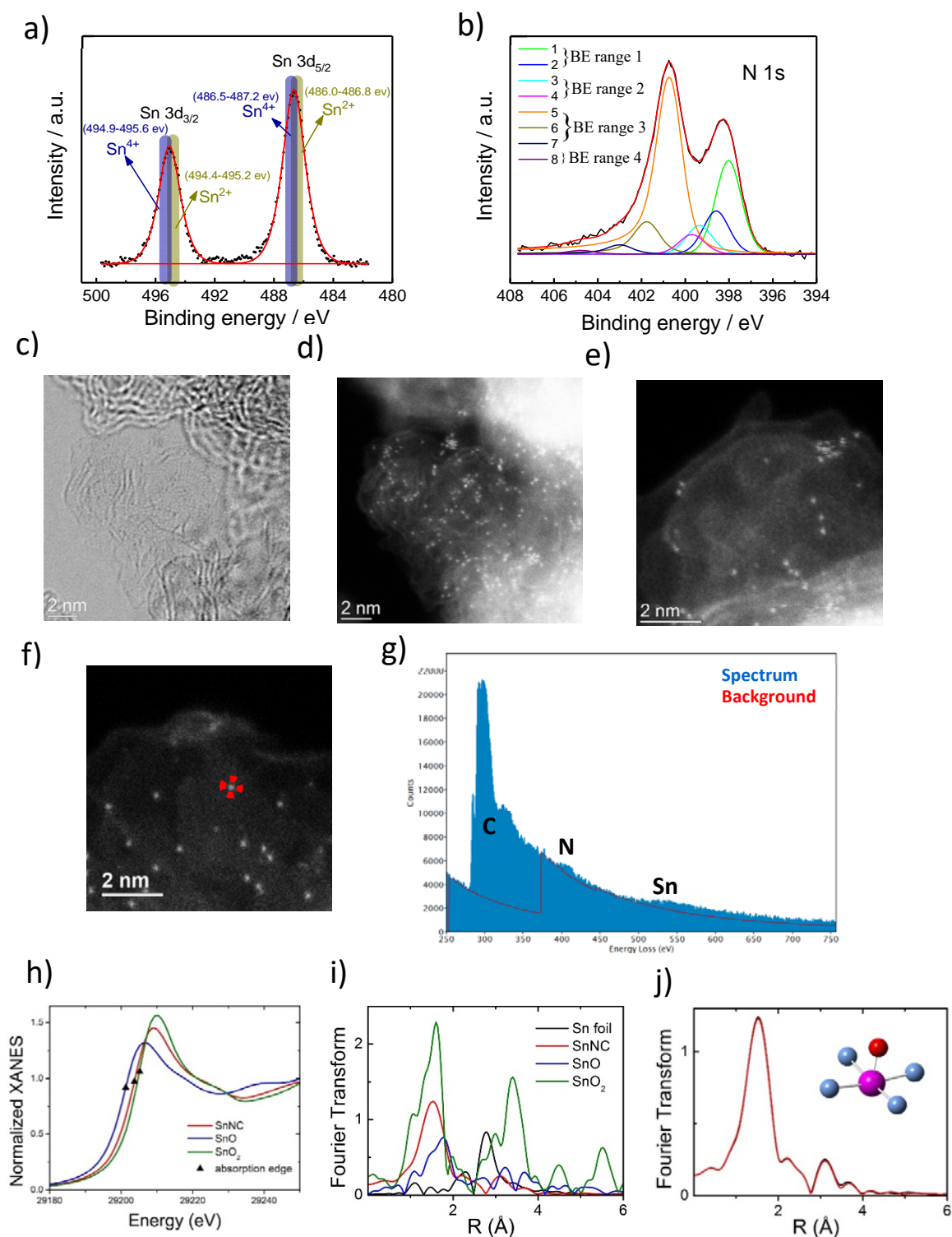
Figure 1. Chemical and structural characterisation of atomically dispersed Sn atoms in SnNC. (a-b) The Sn_{3d} and N_{1s} narrow-scan spectra of SnNC and their fitting. N_{1s} spectral fitting involved eight spectral components segmented into 4 binding energy (BE) ranges (BE-range 1-4) characterized by typical N motifs.

Details see the supplementary online information. (c) BF-STEM image of SnNC. (d-e) HAADF-STEM image identifying bright Sn atoms atomically dispersed in or on graphene layers. (f) HAADF-STEM image and (g) the corresponding local chemical environment near the Sn atom identified by red arrows in (f), as probed by EEL spectrum. (h) Comparison between the Sn K-edge XANES experimental spectrum of SnNC (red curve), SnO (blue curve), and SnO_2 (dark green curve). Black triangles identify the experimental edge positions. (i) Fourier transform of the experimental EXAFS spectra of crystalline tin (black curve), SnNC (red curve), SnO (blue curve), and SnO_2 (dark green curve). j) Sn K-edge EXAFS analysis in the Fourier Transformed space of SnNC. Black and red curves are the experimental and theoretical spectra, respectively. Metal, nitrogen (or carbon) and oxygen atoms are represented in purple, blue and red, respectively (second-shell carbon atoms are not represented). The indicated radial distance is not corrected for phase-shift.

The threshold energy of the Sn K-edge XANES spectrum of SnNC is situated between those for Sn(II)O and Sn(IV)O_2 (**Figure 1h**), in line with our conclusions from XPS. The Fourier transform (FT) of the SnNC EXAFS spectrum (**Figure 1i**) shows the dominant contribution of a first-shell peak at 1.52 Å (uncorrected for phase shift) associated with the coordination of light atoms. No strong contribution is seen at 2.8 and 3.4 Å that would be characteristic for metallic tin and SnO_2, respectively. The Sn K-edge EXAFS spectrum of SnNC was then fitted assuming a variable number of N or C atoms in-plane with Sn (EXAFS cannot distinguish N from C atoms), and of axial oxygen atoms. The fitting identifies four in-plane first-shell N or C atoms at 2.06 Å and one axial oxygen atom at 2.13 Å (**Figure 1j**, **Table S4**). The Sn-N (or Sn-C) distance is comparable to that of Sn-N in Sn(IV) phthalocyanines, characterized by a perfectly planar Sn-N_4 coordination[21, 22, 23]. The remainder of the FT-EXAFS spectrum is well reproduced by second-shell carbon atoms, while the peak at 3.1 Å is due to a minor Sn-Sn contribution with fitted bond distance of 3.28 Å, corresponding to SnO_2 (**Figure S5, Table S4** and supporting text 0).

Catalytic Reactivity, Selectivity, and Stability

The electrocatalytic oxygen reduction activity and selectivity of SnNC, FeNC, CoNC, and a metal-free NC reference were investigated in 0.1 M $HClO_4$ using a Rotating Ring-Disk electrode (RRDE) setup. The linear voltammetry scan of the four catalysts is shown in **Figure 2a.** The top of **Figure 2a** shows that the catalytic selectivity for the 4-electron reduction of oxygen to water drops in the order FeNC > SnNC >> CoNC ~ NC. Thus, while being active for the ORR, CoNC predominantly reduces O_2 in a 2-electron process to H_2O_2 in acidic medium, due to weak binding between Co(II)

and O_2. We showed recently that this CoNC catalyst is in fact very promising for efficient electrochemical H_2O_2 production[24]. In contrast, Fe(II) centers bind O_2 stronger, favoring the 4-electron ORR process[6, 9, 25]. The binding energy between metal cations and O_2 , however, not only impacts selectivity but also the intrinsic activity of MN_x sites[26], and thus, the observed Tafel behavior (**Figure S6a**). Comparisons of catalyst mass activities (**Figure S6b**), j_m, of PGM-free MNC materials, always need to account for the differences in the metal atomic contents, as well (Details in Supplementary Information). In the present case, FeNC displayed a roughly 2x higher molar metal content than SnNC (**Table S1**), which renders the metal atom-based catalytic activity of SnNC fully on par with the FeNC catalyst. This is the first report of a new p-block metal-based MNC catalyst rivaling the 4e$^-$ ORR reactivity of FeNC in acidic electrolytes. Beyond catalytic activity, high cycling stability of a MNC catalyst at varying applied electrode potentials is a first criterion for the catalytic durability of SnNC (see **Figure S7**). The catalyst performance loss calculated from linear regression was 3 to 13% after 4.500 RDE cycles and 5 to 10% after 9,000 cycles. The ORR activity of SnNC with atomically dispersed Sn has not been previously reported and is the key feature of the present study[27, 28, 29].
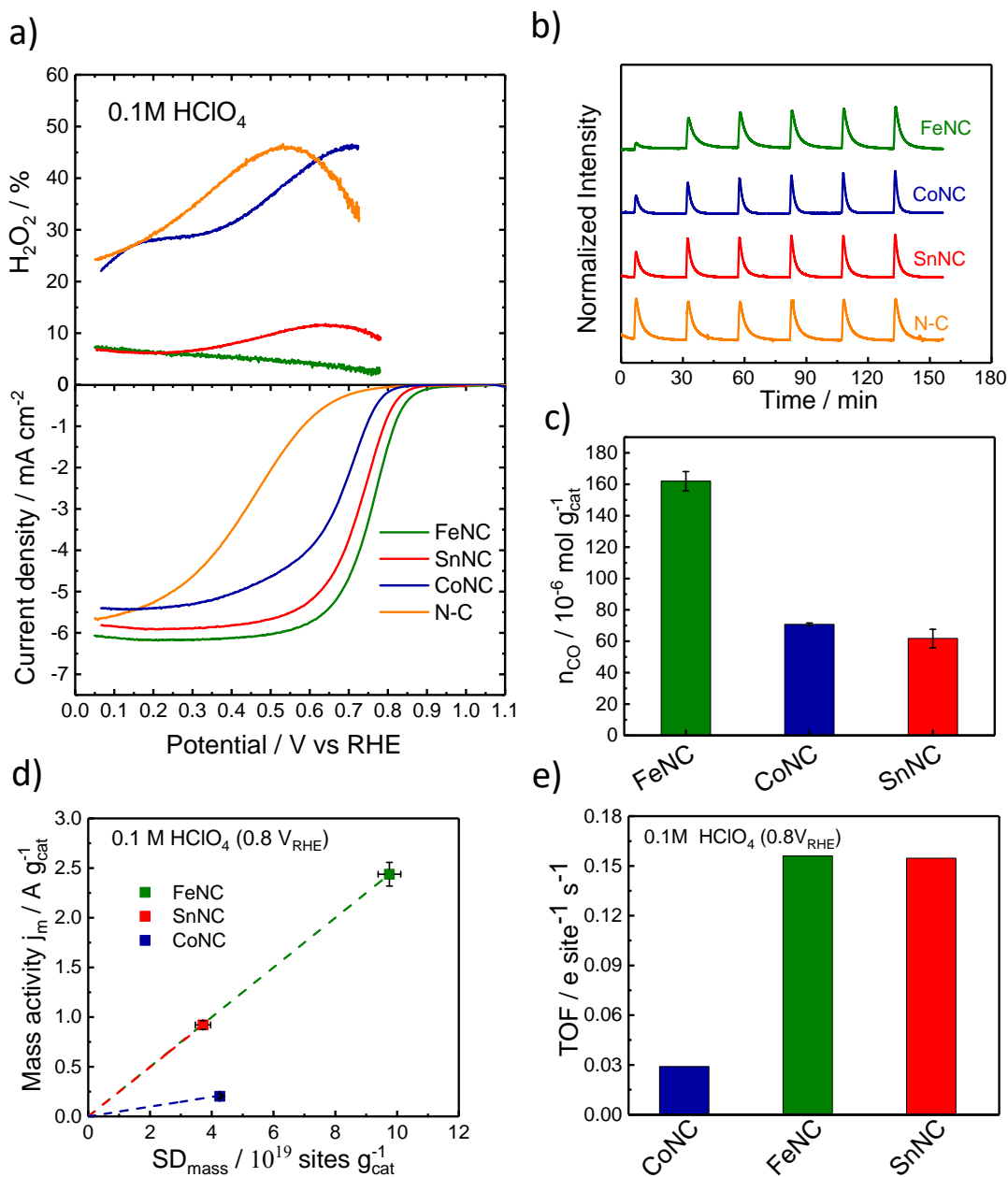
Figure 2. Electrochemical ORR activity, selectivity, active site density and TOF for selected MNC catalysts and for NC. (a) steady-state ORR polarization plots and selectivity in O_2-saturated 0.1 M $HClO_4$ electrolyte, showed the characteristic exponential current density vs potential behavior in the kinetically controlled region, i.e. charge transfer is rate determining, at the most positive applied electrode potentials of 1.0-0.8 V_{RHE} (lowest ORR overpotentials), the mixed kinetic-diffusion region (0.8-0.6V), followed by the oxygen diffusion limited current plateau at low electrode potentials (< 0.6 V_{RHE}). (b) Carbon monoxide pulse chemisorption profiles. (c) Moles of carbon monoxide that chemisorbed per mg catalyst. (d) ORR

mass activity at 0.8 V *vs*. RHE as a function of the site density measured by CO cryo-sorption. (e) Comparison of TOF values for ORR at 0.8 V_{RHE}.

Intrinsic turn over frequency (TOF) and the density of active metal surface sites

To deconvolute the experimental ORR mass activities into the intrinsic reactivity (TOF) and the surface density of the single-metal $Sn-N_x$ sites, we applied cryo CO-pulse chemisorption. This technique has already proven its ability to quantify the number of surface-exposed metal sites for FeNC, MnNC and bimetallic FeMnNC system[9, 30]. The number of sites per catalyst mass (SD_{mass}) follows directly from the molar CO uptake per catalyst mass (n_{CO}), assuming one CO molecule adsorbs per metal site (see Eq. 1 in Supplementary Information). **Figure 2b** displays the CO uptake during six consecutive pulses for each of the four materials of interest (also see **Figure S8a**). The lack of change in the pulse areas of NC indicates negligible CO adsorption in absence of metal centers (**Figure 2b**). In contrast, FeNC, SnNC and CoNC showed significant CO chemisorption (**Figure S8b**). The catalyst n_{CO}, is shown in **Figure 2c and Table S5**, revealing FeNC adsorbed about twice as much CO than SnNC by weight, followed by CoNC. The n_{CO}, can be readily converted into a metal surface site density, SD_{mass}. The slopes of the linear relations between j_m SD_{mass}, (**Figure 2d**) yielded the intrinsic ORR TOF values of FeNC, SnNC, and CoNC (see Eq. 2 in Supplementary Information and **Figure 2e**). While CoNC showed a TOF of 0.029 e site^{-1}s^{-1}, the TOFs of FeNC and SnNC were essentially identical and 5x larger around 0.15 e site^{-1}s^{-1}, confirming SnNC as a novel ORR catalyst system of great importance for acidic PEM conditions (**Table S6**). The data also explained why SnNC showed a slightly lower catalyst mass activity than FeNC, due namely to its lower SD_{mass} ensuing from the larger molar mass of Sn. Clearly, other factors may weigh in (see Supporting text 1) such as the porosity or specific areas of SnNC and FeNC: SnNC showed a roughly 2x lower microporous and BET surface area compared to FeNC (**Figure S9**, **Table S7**). This implies that, per unit area of carbon, the density of SnN_x and FeN_x sites are, in fact, nearly same.

The ORR activity volcano and chemisorption relations

Atomically dispersed Sn cations covalently integrated in a N-doped carbon matrix constitute a new class of MNC materials. Containing a p-block element, the reactivity of the Sn-based SnN_x single

metal moieties at the surface of the catalyst may be subjected to a distinctly different reactivity than the conventional 3d metal-containing MN_x moieties. In particular, p-block based SnN_x moieties appear not to completely follow the conventional chemisorption correlation between reactive intermediates (**Figure 3**). Using DFT modeling, we analyzed the structure - reactivity relationship (**Figure 3a**) of eight distinct single metal SnN_x sites in graphene, with varied first coordination sphere. Four pyridinic SnN_xC structures ($1 \leq x \leq 4$, structures 1-4), four SnN_xC porphyrinic clusters ($1 \leq x \leq 4$, structures 5-8), metallic Sn fcc(111) slab (structure 9) and SnO_2 (structure 10) were considered (**Figure 3c**). In order to verify first the reliability of DFT modeling, similar calculations were performed for Fe, Co, Ni, Cu single sites assuming the MN_4C pyridinic structure, that we have previously shown to be an accurate representation of the active sites[24]. We compare computational (DFT) and experimental activities (RRDE) using a volcano ORR activity plot in **Figure 3a**[31, 32]. The left hand side y-axis reports the onset electrode potential derived from the calculated rate-determining step identified in the ORR associative pathway[31, 33], while the right hand side y-axis shows the experimental disk and ring currents (**Figure S10** and **Table S8**). The logarithmic scale is used for currents (Tafel law)[34]. To highlight possible trend deviations over the set of catalysts, Fe is chosen as reference point, as detailed in supporting text 2. The trend for the transition metal MN_4C structures (M = Fe, Co, Cu, Ni) shows excellent agreement between theory and experiments (**Figure 3a,b**), confirming our previous works[24, 31]. One slight mismatch is observed only for NiN_4C and discussed in Supporting Information (**Figure S8 and S10**).
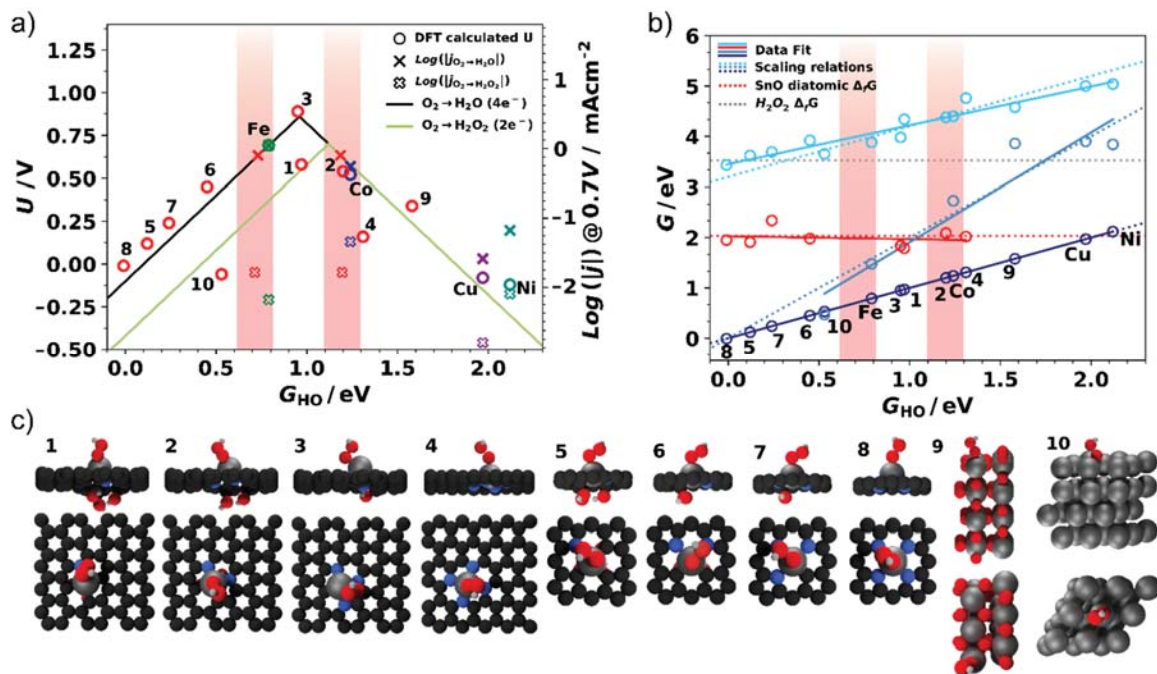
Figure 3. Volcano relationship, chemisorption relations and Sn motifs. a) The ORR volcano activity plot. Computed onset potential (circles, left-hand side y-axis) and logarithm of the experimental RRDE currents corresponding to the 4e$^-$ and 2e$^-$ ORR (thin and thick crosses respectively, right-hand side y-axis) *vs.* the chosen reaction descriptor G_{HO}. The numeric labels correspond to the different SnN$_x$C motifs reported in c). The solid lines (coloured lime and black for 2e$^-$ and 4e$^-$ pathway, respectively) indicate the ORR thermodynamic limits. The solid lines overlap at the volcano right-hand side, for the O$_2$ → *OOH adsorption step is common in both pathways. Two distinct lines define the desorption step limit, being either *OH → H$_2$O (4e$^-$) or *OOH → H$_2$O$_2$ (2e$^-$). The fading red vertical bands at 0.71 eV and 1.20 eV highlight the ideal G_{HO} values for SnN$_x$C, for which the experimental value Log(J$_{disk}$) for SnNC would follow the volcano activity relationship, as the other d-block metals do. **b)** Chemisorption strength correlations between ORR reactive intermediates (*OOH, *O and *OH) on all investigated Sn motifs in c) and transition metals single sites (MN$_4$C, pyridinic N) in the study. The solid and dashed lines represent the ideal theoretical correlations and the linear fit across computed data points, respectively, for *OH *vs.* *OH (navy), *O (teal blue), *OOH (light blue). The altered correlation *OH *vs.* *O for SnN$_x$C is shown in red. **c)** The investigated Sn structures, here shown with *OOH adsorbate, with truncated C terminations in proximity of Sn sites were passivated with hydroxyl groups (structures 1-3 and 5-7).

To investigate the origin of SnNC activity further, we assumed the catalysts should follow the other elements trend along the volcano relationship. By crossing the experimentally measured Log(j) data for SnNC with the volcano thermodynamic lines, we identify two possible G_{HO} values, 0.71 and 1.20 eV, represented as red vertical bands in **Figure 3a-b**. Their width embodies the uncertainty intrinsic to DFT[31, 32, 35]. We thereby established two possible scenarios for SnN$_x$C to exist coherently within our model, one as a catalyst that is limited by strong oxygen chemisorption (left band), and a second case, where the SnNC is limited by too weak oxygen chemisorption (right band). The comparison of binding strength (G_{HO}) of specific, selected SnN$_x$C motifs with the red bands allowed us to suggest the likely nature of the active site from the pool of considered motifs. The model rules out tin oxide (9) and metallic Sn (10) as active species in SnNC. The porphyrinic motifs (structures 5-8) generally lead to binding properties stronger than ideal (**Figure 3a, Figure S11**), yielding computed rate mismatch with experimental Log(j_{disk}). In contrast, the pyridinic motifs (1-4) lead to computed rate and G_{HO} more legitimate. Specifically, structure 3 computed rate is close to the ORR maximum, while structure 1 and 2 computed rates approach best the SnNC Log(j_{disk}) within the model, with 2 fully satisfying the G_{HO} criterion at the weak red band, details discussed in Supporting Information.

All considered SnN$_x$C motifs presented chemisorption values deviating the commonly accepted theory (the scaling relationships, established previously[16, 17, 18] and here reported in **Figure 3b** as dashed lines). This could be due to the different coordination chemistry of the p-block active site. In fact, none of the structures 1-8 in **Figure 3b** follows the ideal correlation G_{HO} *vs.* G_O, common for the ORR associative pathway over a wide range of materials[15, 16, 17, 18], while Sn metal and SnO$_2$ (structures 9 and 10, **Figure 3b**) do, together with the 3d transition metal MN$_4$C structures. We found G_O to be constant across the screened SnN$_x$ motifs, with a value equal to the free energy of formation for molecular SnO in gas phase (~2 eV, dotted red curve in **Figure 3b**). We suggest this behavior is due to a weaker coordination of the Sn ion upon *O adsorption, ultimately yielding a NC defect held in place by long range interactions such as Van der Waals forces (well represented by the chosen exchange correlation functional BEEF-vdW[36]). Structures 2 and 4 bind *O stronger than ideal chemisorption relations would predict[18]. Their activity is thus limited by the elementary reaction step *O → *OH. Motif 2 is instead a stronger binding catalyst relative to 4, thus overpotential losses on 2 are minimized. More importantly, as consequence of constant $G_O \approx 2eV$,

weakly binding sites such as 2 maintain a significant driving force for the O-O bond cleavage and *O formation (cf. red and grey dot lines in **Figure 3b**). This explains why, although the G_{HO} for structure 2 and CoN_4C are comparable, 2 is significantly more selective towards $4e^-$ ORR.

The local electronic environment of single Sn sites in SnNC

Following the DFT insights, Sn atoms in pyridinic N defects with a low coordination number are presumably the catalyst active sites for ORR. We then searched for additional experimental proof for their presence in SnNC. To this end, we performed experimental and computational ^{119}Sn Mössbauer spectroscopy. In contrast to ^{57}Fe Mössbauer spectroscopy widely applied to study FeNC materials for ORR[11, 37, 38, 39], ^{119}Sn Mössbauer spectroscopy has hitherto not been used to study SnNC catalysts comprising atomically-dispersed Sn. The ^{119}Sn Mössbauer spectrum of SnNC (**Figure 4**) was fitted with four doublets and one singlet, whose isomer shift (IS) and quadrupole splitting (QS) are shown in **Table S9** (the fittings and Mössbauer fitting parameters obtained with an alternative fitting strategy involving a doublet component with high QS are shown in **Figure S12** and **Tables S10-S11** for both SnNC and SnNC-NH$_3$. This alternative fitting was not preferred due to the lack of theoretical support for such a high QS for SnN$_x$ moiety, as exaplined in the caption of Table S9). The components with IS-values of ca 0 and 3.3 mm s^{-1} are unambiguously assigned to Sn(IV) and Sn(II) species, respectively[40]. Sn(IV)-b has IS and QS values matching those of SnO$_2$[41], in line with the identification of a minor content of SnO$_2$ by EXAFS analysis. Sn(II)-b has IS and QS values matching those of Sn(II)-phthalocyanine[42], or of SnS[43]. The presence of SnS, despite the presence of sulfur (**Table S12**), remained doubtful due to the multiple hot acid washings performed in the synthesis of SnNC. The Sn(IV)-a and Sn(II)-a quadrupole components are assigned to atomically-dispersed Sn(IV) and Sn(II) sites, respectively (further discussed after DFT calculations of QS-values). Last, the component D2 (Mixed ionic/covalent) with IS of 1.26 mm·s^{-1} cannot be unambiguously assigned to II or IV oxidation state. Such IS-value is found for Sn-compounds with electronic density at the Sn nucleus situated between that of pure Sn(II) and Sn(IV) compounds[43, 44, 45]. The IS value of D2 matches well for example with SnS$_2$ or Sn$_2$S$_3$[45], surface-oxidized SnS nanocrystals[43], and for Sn-porphyrins forming a complex with Fe(CO)$_4$[44]. Overall, the coexistence of Sn(IV) and Sn(II) species identified by Mössbauer spectroscopy is in line with XPS and XANES results, and the atomic dispersion of

most of the Sn atoms shown by STEM and EXAFS analysis implies that the majority of the [119]Sn Mössbauer components must correspond to atomically-dispersed Sn moieties.
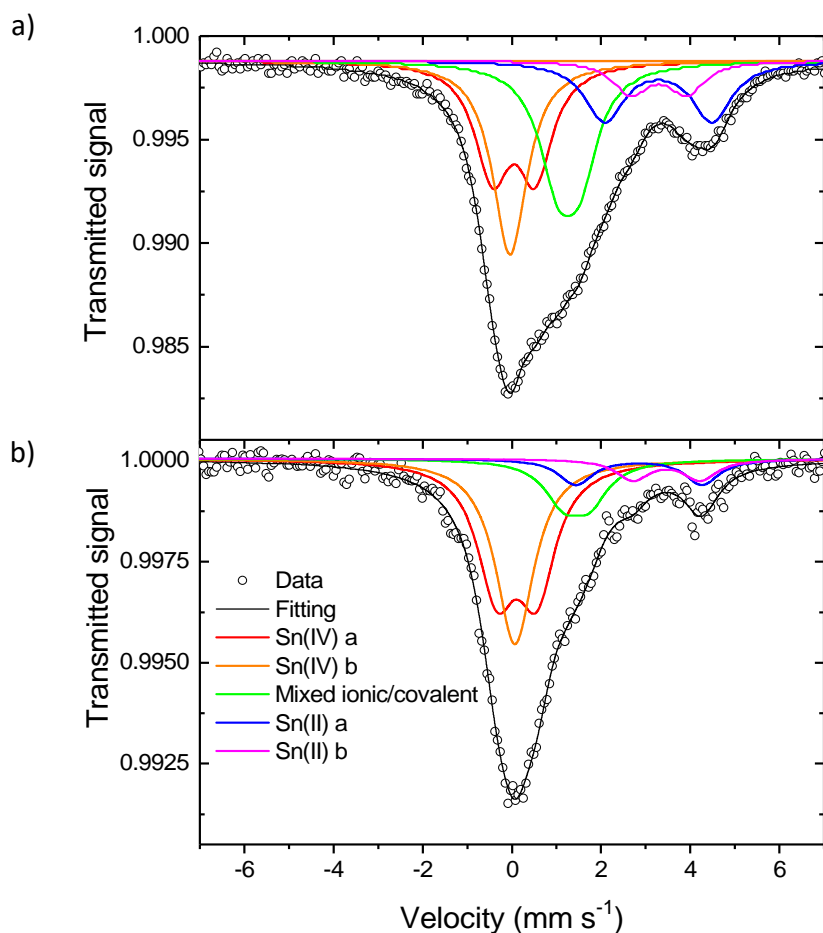

Figure 4.[119]Sn Mössbauer spectroscopy characterization. (a) [119]Sn Mössbauer spectrum of SnNC and (b) [119]Sn Mössbauer spectrum of SnNC-NH$_3$. The spectra were measured at 300 K and the velocity scale was calibrated with BaSnO$_3$ at 300 K. The spectra were fitted with five spectral components and the Mössbauer parameters of each fitted component are reported in Table S9 and S14 for SnNC and SnNC-NH$_3$, respectively. The fitting strategy is explained in the Supplementary information.

Using our recently reported method for FeNC[19], we predicted the QS-values for the SnN_x structures 1-8 in **Figure 3** and **Figure S13** (details in Supplementary Information). Since the spectrum of SnNC was recorded in ambient conditions, we also calculated the QS-values for the same structures after approaching one O_2 molecule, such structures being henceforth labelled as $O-SnN_x$. The calculated QS-values for the SnN_x and $O-SnN_x$ structures are shown in **Table S13**. The results indicate that the Sn centers strongly adsorb O_2, even almost splitting the O-O bond spontaneously (*e.g.* structures 2 and 4, with O-O bond distances of *ca* 1.6 Å, **Figure S14**). SnN_x structures 1, 2, 4, 8 with adsorbed O_2 lead to calculated QS-values in the range 0.9-1.2 mm·s^{-1}, matching the experimental QS-value of the component Sn(IV)-a (0.97 mm·s^{-1}). The strong theoretical adsorption of O_2 on such SnN_x structures is in line with a +IV oxidation state for surface exposed SnN_x moieties. Without O_2 adsorbed, higher QS-values are calculated for all structures, ranging from 1.6 to 2.7 mm·s^{-1} (**Table S13**), except for structure 8. Taking into account a precision of *ca* 0.4 mm s^{-1} on the calculated QS[19], the structures 1-2, 5-7 have QS values (2.4-2.7 mm s^{-1}) that match the experimental QS value for Sn(II)-a (2.41 mm s^{-1}) while structures 3-4 and 8 have calculated QS-values (0.9-2.0 mm s^{-1}) that match the Sn(II)-b component (1.24 mm s^{-1}). In summary, the site structural features (pyridinic N, low N coordination number) suggested by DFT for the active sites lead to QS-values that match with the experimental QS-values observed for the stannic ($O-SnN_2$/C) and stannous component (SnN_2/C). The coexistence of both stannous and stannic SnN_x sites in SnNC may be due to the inaccessibility by O_2 of a fraction of Sn sites, while those located on top surface would bind O_2, giving rise to a doublet with low isomer shift.

Polymer Electrode membrane fuel cell tests

To demonstrate the viability of the new SnNC catalyst in real devices, hydrogen/oxygen PEMFC measurements were carried out using SnNC, FeNC and the reference CoNC catalysts (see Methods). **Figure 5a** demonstrates a much higher performance in the kinetic region of the PEMFC polarization curves (E ≥ 0.7 V) for SnNC and FeNC compared to CoNC, in full accord with the RRDE measurements. SnNC showed a somewhat higher activity in the real fuel cell compared to FeNC. The SnNC cathode further reached significantly higher current densities than the FeNC cathode at low cell voltages. The fuel cell performance along its full polarization curve is a

convoluted reactivity characteristic depending upon interfacial charge transfer (activation or kinetic), ohmic, and mass and charge transport losses, among other parameters. At high cell voltages, however, chemical modification of the active metal single sites can be linked to the resulting current density variations. NH_3 activation of the catalyst is a well-known treatment of MNC catalysts that is known to modify the local Lewis basicity at and around the single site thereby enhancing the TOF of FeN_x active sites[11]. **Figure 5b** shows PEMFC polarization curves plotted as E *vs*. log(j) for the pristine as well as NH_3-activated catalysts (labelled "MNC-NH$_3$"). As expected for FeNC, NH_3 activation resulted in a more than one order-of-magnitude increase in current density at E > 0.75 V (**Figure 5b**, dashed green curve). Surprisingly, SnNC-NH$_3$ not only exhibited a similar enhancement, but also exceeded the state of art FeNC-NH$_3$ catalysts by 40-50% in terms of the measured fuel cell current density at cell voltages lower than 0.7 V (**Figure S15**). In contrast, CoNC and CoNC-NH$_3$ showed comparable activities at low cell voltage (**Figure 5b**), with a slight improvement in activity at high cell voltages likely thanks to the slightly increased surface area resulting from an etching effect of NH_3. Again, the reactivity of SnNC and FeNC followed similar patterns, however, SnNC turned out superior to the state of art FeNC catalyst in the real fuel cell device.
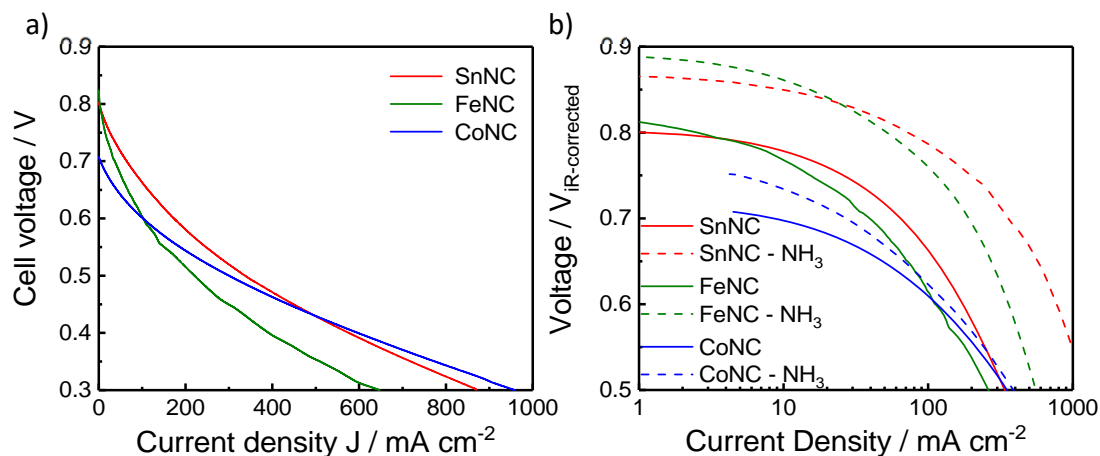
Figure 5. Fuel cell measurements. (a) PEMFC polarization curves for pristine SnNC, FeNC, and CoNC and (b) iR-corrected polarization curves presented as Tafel plots, comparing the pristine catalysts (solid curves) to the NH_3-activated catalysts (dashed curves). The cathode loading was 4 mg cm^{-2} and the anode loading was 2.0 mg$_{Pt}$ cm^{-2}. The cell temperature was 80 °C, H_2 and O_2 with 100% relative humidity (RH) was flowed on each side and the gas pressure was 2 bar absolute on each side. Polarization curves were acquired using linear scan voltammetry with a scan rate of 1mV·s^{-1}.

^{119}Sn Mössbauer spectroscopy of SnNC-NH_3 offered further molecular insight into the origin of the beneficial PEMFC performance following the NH_3 activation. While similar spectral components are seen for SnNC and SnNC-NH_3 (**Figure 4a and 4b, respectively**), the strongly reduced relative intensity of the green doublet and stannous components in SnNC-NH_3 lend support to the hypothesis that the stannic components are responsible for the ORR activity. In particular, Sn(IV)-a, assigned as atomically dispersed Sn(IV)-N_x active sites with axially adsorbed oxygen, was found to increase by 16 rel.% after NH_3 activation, making it a good candidate as the most active site in SnNC and SnNC-NH_3. Further, the increase in Sn(IV)-a signal is inversely proportional to the relative decrease in D2 signal, assigned as mixed ionic/covalent species, with spectral signature similar to that of surface-oxidized SnS nanoparticles (**Table S14**). This suggests the possible conversion of inorganic Sn phases to atomically-dispersed Sn(IV)N_x sites during pyrolysis. The conversion of Fe nano-oxides into FeN$_x$ sites during pyrolysis was recently reported[46, 47]. Also, the relative decrease in the Sn(II)-a component (assigned to Sn(II)N$_x$ sites) and possible transformation into the Sn(IV)-a component suggests that NH_3–activation may have brought to the surface (via carbon etching) some sites that were previously buried in the carbon

matrix. However, the increase in the signal intensity of the Sn(IV) Mössbauer components from SnNC to SnNC-NH$_3$ is negligible compared to the activity improvement observed in PEMFC measurements (activity x 10 for SnNC-NH$_3$ vs. SnNC). Therefore, the higher activity of SnNC-NH$_3$ vs. SnNC can be ascribed to an increased TOF of Sn-based surface sites, as a result of modified Lewis basicity of N-C by ammonia activation and ensuing modified chemisorption of oxygenated intermediates on the single SnN$_x$ surface sites.

Conclusions

This contribution reports the discovery and analysis of PGM-free, p-block Sn-based single metal site MNC catalysts for the electroreduction of molecular oxygen at fuel cell cathodes. This is the first report of a new MNC catalyst rivaling the 4e- ORR reactivity of FeNC in acidic electrolytes. Surprisingly, the catalytic active central metal is one of the p-block of the periodic Table with closed d shells, what typically limits surface catalytic reactivity in transition metals. In the d-block, partially-filled d-bands lie across the Fermi level and their band center relative to the Fermi level control the strength of the bond with the adsorbates.[48, 49] The SnNC catalysts meet and exceed state of art FeNC catalysts in terms of intrinsic catalytic TOF and fuel cell power density[50]. The SnNC catalysts displayed a 40-50% higher current density than FeNC-NH$_3$ at cell voltages below 0.7 V, and a high favorable selectivity for the 4 electron reduction pathway (**Table S15**).

Molecular insights into the catalytic active sites of the SnNC catalyst were obtained using a combination of different analytical techniques with DFT computations: Single Sn-N$_x$ sites were confirmed by High Resolution STEM-EELS to be atomically dispersed, while Mössbauer and XAS spectroscopy evidenced stannic components Sn(IV)-N$_x$ as the active single metal sites. Experimental conclusions were supported by first principle DFT calculations. They ruled out metallic or oxidic Sn-species as the catalytically active site, but rather suggested pyridinic N–coordinated Sn atoms embedded in the carbon matrix as the most likely catalytic single metal site. DFT results also indicated deviation from the theoretical oxygen chemisorption strength correlation in the Sn-N$_x$-O system: All SnNC structures screened displayed an essentially constant oxygen chemisorption energy, G$_O$, of ~ 2 eV, that is, well below the formation energy of H$_2$O$_2$ (3.56 eV). This rationalized the experimentally observed high 4e$^-$ selectivity of SnNC catalysts

regardless of the active site exact nature. The discovery that Sn-based MNC are highly active, selective, catalysts for the ORR expands the known set of viable PGM-free fuel cell cathode catalysts beyond today's default Fe and/or CoNCs, possibly constituting a promising substitute for expensive Pt catalysts in PEMFC cathodes.

References

1.   Wong KH, Kjeang E. Mitigation of Chemical Membrane Degradation in Fuel Cells: Understanding the Effect of Cell Voltage and Iron Ion Redox Cycle. *ChemSusChem* 2015, **8**(6)**:** 1072-1082.

2.   Atsushi Ohmaa KS, Akihiro Iiyamaa,Toshihiko Yoshidab and Akimasa Daimaru. Membrane and Catalyst Performance Targets for Automotive Fuel Cells by FCCJ Membrane, Catalyst, MEA WG. *ECS Transactions* 2011, **41**(1).

3.   Holton OT, Stevenson JW. The Role of Platinum in Proton Exchange Membrane Fuel Cells. *Platinum Metals Review* 2013, **57**(4)**:** 259-271.

4.   Zhang S, Yuan X-Z, Hin JNC, Wang H, Friedrich KA, Schulze M. A review of platinum-based catalyst layer degradation in proton exchange membrane fuel cells. *Journal of Power Sources* 2009, **194**(2)**:** 588-600.

5.   Lefevre M, Proietti E, Jaouen F, Dodelet JP. Iron-based catalysts with improved oxygen reduction activity in polymer electrolyte fuel cells. *Science* 2009, **324**(5923)**:** 71-74.

6.   Wu G, More KL, Johnston CM, Zelenay P. High-Performance Electrocatalysts for Oxygen Reduction Derived from Polyaniline, Iron, and Cobalt. *Science* 2011, **332**(6028)**:** 443-447.

7.   Bashyam R, Zelenay P. A class of non-precious metal composite catalysts for fuel cells. *Nature* 2006, **443**(7107)**:** 63-66.

8.   Jiang WJ, Gu L, Li L, Zhang Y, Zhang X, Zhang LJ*, et al.* Understanding the High Activity of Fe-N-C Electrocatalysts in Oxygen Reduction: Fe/Fe3C Nanoparticles Boost the Activity of Fe-N(x). *Journal of the American Chemical Society* 2016, **138**(10)**:** 3570-3578.

9.   Sahraie NR, Kramm UI, Steinberg J, Zhang Y, Thomas A, Reier T*, et al.* Quantifying the density and utilization of active sites in non-precious metal oxygen electroreduction catalysts. *Nat Commun* 2015, **6:** 8618.

10.   Bezerra CWB, Zhang L, Lee K, Liu H, Marques ALB, Marques EP*, et al.* A review of Fe–N/C and Co–N/C catalysts for the oxygen reduction reaction. *Electrochimica Acta* 2008, **53**(15)**:** 4937-4951.

11.   Zitolo A, Goellner V, Armel V, Sougrati M-T, Mineva T, Stievano L*, et al.* Identification of catalytic sites for oxygen reduction in iron- and nitrogen-doped graphene materials. *Nat Mater* 2015, **14**(9)**:** 937-942.

12. Chung HT, Cullen DA, Higgins D, Sneed BT, Holby EF, More KL, *et al.* Direct atomic-level insight into the active sites of a high-performance PGM-free ORR catalyst. *Science* 2017, **357**(6350)**:** 479-484.

13. Zitolo A, Ranjbar-Sahraie N, Mineva T, Li J, Jia Q, Stamatin S, *et al.* Identification of catalytic sites in cobalt-nitrogen-carbon materials for the oxygen reduction reaction. *Nature Communications* 2017, **8**(1)**:** 957.

14. Raymond J. A new fuel cell cathode catalyst. *Nature* 1964, **201**(492)**:** 1212-1213.

15. Nørskov JK, Rossmeisl J, Logadottir A, Lindqvist L, Kitchin JR, Bligaard T, *et al.* Origin of the Overpotential for Oxygen Reduction at a Fuel-Cell Cathode. *The Journal of Physical Chemistry B* 2004, **108**(46)**:** 17886-17892.

16. Koper MTM. Thermodynamic theory of multi-electron transfer reactions: Implications for electrocatalysis. *Journal of Electroanalytical Chemistry* 2011, **660**(2)**:** 254-260.

17. Man IC, Su H-Y, Calle-Vallejo F, Hansen HA, Martínez JI, Inoglu NG, *et al.* Universality in Oxygen Evolution Electrocatalysis on Oxide Surfaces. *ChemCatChem* 2011, **3**(7)**:** 1159-1165.

18. Viswanathan V, Hansen HA, Rossmeisl J, Nørskov JK. Universality in Oxygen Reduction Electrocatalysis on Metal Surfaces. *ACS Catalysis* 2012, **2**(8)**:** 1654-1660.

19. Mineva T, Matanovic I, Atanassov P, Sougrati M-T, Stievano L, Clémancey M, *et al.* Understanding Active Sites in Pyrolyzed Fe–N–C Catalysts for Fuel Cell Cathodes by Bridging Density Functional Theory Calculations and 57Fe Mössbauer Spectroscopy. *ACS Catalysis* 2019, **9**(10)**:** 9359-9371.

20. Wagner S, Auerbach H, Tait CE, Martinaiou I, Kumar SCN, Kubel C, *et al.* Elucidating the Structural Composition of an Fe-N-C Catalyst by Nuclear- and Electron-Resonance Techniques. *Angewandte Chemie* 2019, **58**(31)**:** 10486-10492.

21. Silver J, Frampton CS, Fern GR, Davies DA, Miller JR, Sosa-Sanchez JL. Novel Seven Coordination Geometry of Sn(IV): Crystal Structures of Phthalocyaninato Bis(undecylcarboxylato)Sn(IV), Its Si(IV) Analogue, and Phthalocyaninato Bis(chloro)silicon(IV). The Electrochemistry of the Si(IV) Analogue and Related Compounds. *Inorganic Chemistry* 2001, **40**(21)**:** 5434-5439.

22. Konarev DV, Troyanov SI, Faraonov MA, Ishikawa M, Otsuka A, Yamochi H, *et al.* Molecular structure, optical and magnetic properties of the {SnIVPc(3-)Cl2}•- radical anions containing negatively charged Pc ligands. *Journal of Porphyrins and Phthalocyanines* 2015, **18**(12)**:** 1157-1163.

23. Das SWNaVGK. Tricyclohexyl[(N,N-diethylthiocarbamoylthio)acetato-O]tin(IV). *Acta Cryst* 1997, **C53:** 548-549.

24. Sun Y, Silvioli L, Sahraie NR, Ju W, Li J, Zitolo A, *et al.* Activity-Selectivity Trends in the Electrochemical Production of Hydrogen Peroxide over Single-Site Metal-Nitrogen-Carbon Catalysts. *Journal of the American Chemical Society* 2019, **141**(31)**:** 12372-12381.

25. Jaouen F, Dodelet J-P. Average turn-over frequency of O2 electro-reduction for Fe/N/C and Co/N/C catalysts in PEFCs. *Electrochimica Acta* 2007, **52**(19)**:** 5975-5984.

26. Zagal JH, Koper MT. Reactivity Descriptors for the Activity of Molecular MN4 Catalysts for the Oxygen Reduction Reaction. *Angewandte Chemie* 2016, **55**(47)**:** 14510-14521.

27. Ramaswamy N, Tylus U, Jia Q, Mukerjee S. Activity descriptor identification for oxygen reduction on nonprecious electrocatalysts: linking surface science to coordination chemistry. *Journal of the American Chemical Society* 2013, **135**(41)**:** 15443-15449.

28. Zagal J. Metallophthalocyanines as catalysts in electrochemical reactions. *Coordination Chemistry Reviews* 1991, **119(1992) 89-136**.

29. Tylus U, Jia Q, Strickland K, Ramaswamy N, Serov A, Atanassov P, *et al.* Elucidating Oxygen Reduction Active Sites in Pyrolyzed Metal–Nitrogen Coordinated Non-Precious-Metal Electrocatalyst Systems. *The journal of physical chemistry C, Nanomaterials and interfaces* 2014, **118**(17)**:** 8999-9008.

30. Luo F, Choi CH, Primbs MJM, Ju W, Li S, Leonard ND, *et al.* Accurate Evaluation of Active-Site Density (SD) and Turnover Frequency (TOF) of PGM-Free Metal–Nitrogen-Doped Carbon (MNC) Electrocatalysts using CO Cryo Adsorption. *ACS Catalysis* 2019**:** 4841-4852.

31. Yang S, Verdaguer-Casadevall A, Arnarson L, Silvioli L, Čolić V, Frydendal R, *et al.* Toward the Decentralized Electrochemical Production of H2O2: A Focus on the Catalysis. *ACS Catalysis* 2018, **8**(5)**:** 4064-4081.

32. Ju W, Bagger A, Hao GP, Varela AS, Sinev I, Bon V, *et al.* Understanding activity and selectivity of metal-nitrogen-doped carbon catalysts for electrochemical reduction of CO2. *Nat Commun* 2017, **8**(1)**:** 944.

33. Jaouen Fdr, Dodelet J-P. O2Reduction Mechanism on Non-Noble Metal Catalysts for PEM Fuel Cells. Part I: Experimental Rates of O2Electroreduction, H2O2Electroreduction, and H2O2Disproportionation. *The Journal of Physical Chemistry C* 2009, **113**(34)**:** 15422-15432.

34. Rossmeisl J, Karlberg GS, Jaramillo T, Nørskov JK. Steady state oxygen reduction and cyclic voltammetry. *Faraday Discussions* 2009, **140**(0)**:** 337-346.

35. Medford AJ, Wellendorff J, Vojvodic A, Studt F, Abild-Pedersen F, Jacobsen KW, *et al.* Assessing the reliability of calculated catalytic ammonia synthesis rates. *Science* 2014, **345**(6193)**:** 197-200.

36. Wellendorff J, Lundgaard KT, Møgelhøj A, Petzold V, Landis DD, Nørskov JK, *et al.* Density functionals for surface science: Exchange-correlation model development with Bayesian error estimation. *Physical Review B* 2012, **85**(23)**:** 235149.

37. Kramm UI, Lefèvre M, Larouche N, Schmeisser D, Dodelet J-P. Correlations between Mass Activity and Physicochemical Properties of Fe/N/C Catalysts for the ORR in PEM Fuel Cell via 57Fe Mössbauer Spectroscopy and Other Techniques. *Journal of the American Chemical Society* 2014, **136**(3)**:** 978-985.

38. Kramm UI, Ni L, Wagner S. (57) Fe Mossbauer Spectroscopy Characterization of Electrocatalysts. *Advanced materials* 2019, **31**(31)**:** e1805623.

39. Kramm UI, Lefèvre M, Bogdanoff P, Schmeißer D, Dodelet J-P. Analyzing Structural Changes of Fe–N–C Cathode Catalysts in PEM Fuel Cell by Mößbauer Spectroscopy of Complete Membrane Electrode Assemblies. *The Journal of Physical Chemistry Letters* 2014, **5**(21)**:** 3750-3756.

40. Gütlich P. Physikalische Methoden in der Chemie: Mößbauer-Spektroskopie I. *Chemie in unserer Zeit* 1970, **4**(5)**:** 133-144.

41. Indris S, Scheuermann M, Becker SM, Šepelák V, Kruk R, Suffner J, *et al.* Local Structural Disorder and Relaxation in SnO2 Nanostructures Studied by 119Sn MAS NMR and 119Sn Mössbauer Spectroscopy. *The Journal of Physical Chemistry C* 2011, **115**(14)**:** 6433-6437.

42. O'Rourke M, Curran BC. Moessbauer spectra of tin complexes of phthalocyanine and tetraarylporphines. *Journal of the American Chemical Society* 1970, **92**(6)**:** 1501-1505.

43. de Kergommeaux A, Faure-Vincent J, Pron A, de Bettignies R, Malaman B, Reiss P. Surface Oxidation of Tin Chalcogenide Nanocrystals Revealed by 119Sn–Mössbauer Spectroscopy. *Journal of the American Chemical Society* 2012, **134**(28)**:** 11659-11666.

44. Barbe JM, Ratti C, Richard P, Lecomte C, Gerardin R, Guilard R. Tin(II) porphyrins: synthesis and spectroscopic properties of a series of divalent tin porphyrins. X-ray crystal structure of (2,3,7,8,12,13,17,18-octaethylprophinato)tin(II). *Inorganic Chemistry* 1990, **29**(20)**:** 4126-4130.

45. Lippens PE. Interpretation of the 119Sn Mössbauer isomer shifts in complex tin chalcogenides. *Physical Review B* 1999, **60**(7)**:** 4576-4586.

46.   Li J, Zhang H, Samarakoon W, Shan W, Cullen DA, Karakalos S, *et al.* Thermally Driven Structure and Performance Evolution of Atomically Dispersed FeN4 Sites for Oxygen Reduction. *Angewandte Chemie* 2019, **58**(52)**:** 18971-18980.

47.   Li J, Jiao L, Wegener E, Richard LL, Liu E, Zitolo A, *et al.* Evolution Pathway from Iron Compounds to Fe1(II)-N4 Sites through Gas-Phase Iron during Pyrolysis. *Journal of the American Chemical Society* 2020.

48.   Hammer B, Norskov JK. Why gold is the noblest of all the metals. *Nature* 1995, **376**(6537)**:** 238-240.

49.   Nørskov JK, Abild-Pedersen F, Studt F, Bligaard T. Density functional theory in surface chemistry and catalysis. *Proceedings of the National Academy of Sciences* 2011, **108**(3)**:** 937-943.

50.   Mathias Primbs PS, Deborah Jones, Frederic Jaouen, Aaron Roy, Pierre-Yves Blanchard, Moulay Tahar Sougrati, Daniel Malko, Anthony Kucernak, Gaetano Granozzi, Christian Durante, Tomasz Kosmala, Valentina Perazzolo, Jonathan Sharman. CRESCENDO Deliverable Report D3.1-Site Density and Turn over frequency of selected benchmark catalysts. http://www.crescendo-fuelcell.eu/index.php/activities/deliverables?jjj=1565098846810; 2018, 05.

Acknowledgements

Author contributions

F.L., P.S. and F.J. conceived, designed and coordinated the study. F.L. carried out the materials synthesis, characterization and electrochemical evaluations. A.R., D.A.C., A.Z., M. T. S., I.C.O., T.M., D.T., S.W., F.D., U.I.K. and F.J.: MEA, STEM/EELS, Sn K-edge EXAFS/XANES, Mössbauer spectroscopy, XPS and Fe L-edge XAS experimental work and data analysis. L.S. and J.R.: DFT computational study. J.W. and F. D. participated in the discussion of the electrochemical results section. All authors discussed the results and commented on the manuscript. F.L. wrote the manuscript with the contribution of all co-authors.

Competing interests

The authors declare no competing interests.

Methods

Catalyst synthesis. Metal chloride ($FeCl_3$, $SnCl_2$, $CuCl_2$, $NiCl_2$), aniline, pretreated carbon support and ammonium peroxydisulfate (APS, $(NH_4)_2S_2O_8$) were used as precursors for preparing the single-metal (Fe, Sn, Cu, Ni)-NC catalysts. Preparation of polyaniline was performed by solving the aniline in 0.5 M HCl with adding the oxidization agent APS, then mix with metal chloride and pretreated carbon support into the complete polymerization suspension. After evaporation of solvents, the catalysts' precursors were processed by ball-milling in a zirconium oxide (ZrO_2) crucible with 10 pieces of 12 mm diameter ZrO_2 balls. The collected dry powder was then pyrolysed in N_2 at 900 °C for 1 hour (heating ramp rate: 5 °C /min), and followed by acid washing step for leaching out the pure metal particles and metal sulfide, then the dry powder was pyrolysed and acid leaching again same as before, then third pyrolysis for achieving the final catalysts. For CoNC synthesis, Zn(II) zeolitic imidazolate framework (ZIF-8), 1,10-phenanthroline and cobalt(II) acetate were used as catalyst precursors. The precursors were homogenized in a planetary ball-miller and flash-pyrolyzed at 1050 °C in Ar flow for 1 h to get the final CoNC catalyst (no acid leaching step). Full details of the synthesis are given in Ref[13].

NH₃ Activation: SnNC, FeNC, and CoNC were further activated by loading 100–200 mg of pristine catalyst into a tubular furnace. The flow rate of anhydrous NH_3 was maintained at ~200 sccm for 2 hours while the furnace was allowed to equilibrate at the activation temperature of 750 or 900℃, with the catalyst powder outside of the heating zone. The activation temperature was optimized for each catalyst, to give the highest PEMFC performance. Once the oven had equilibrated at the set temperature (i.e. 2 h of equilibration once the temperature indicator reached the set temperature), the catalyst powder was inserted in *ca* 30 s in the heating zone with an outer magnet, by pushing a quartz rod/magnet assembly, previously installed inside the quartz tube. The NH_3 activation was carried out for 5 min, and the split hinge furnace was then opened and quartz tube removed to quench the temperature and stop the NH_3 activation. This flash pyrolysis process is fully described in Ref[51].

Physical characterization. XPS and soft X-ray XAS experiments were performed at the ISISS beamline of the synchrotron facility BESSY of the Helmholtz-Zentrum Berlin under room temperature in ultra-high vacuum. Atomic-resolution images of atomically-dispersed Sn sites in SnNC were captured by aberration-corrected scanning transmission electron microscopy (STEM) using a Nion UltraSTEM 100 operated at 60 kV and equipped with a Gatan Enfina electron energy loss spectrometer. Mössbauer spectroscopy measurements were acquired on SnNC and FeNC in transmission mode at room temperature, and the spectra fitted with appropriate combination of Lorentzian profiles by least-square methods. XAS

measurements were carried out at room temperature in transmission geometry at the SAMBA beamline (Synchrotron SOLEIL).

Electrochemical Measurements. Rotation-Ring disk electrode (RRDE) measurements were performed to determine the ORR activity and selectivity of MNC catalysts in acidic liquid electrolyte. 15.7 mg catalyst powder, 750 µl de-ionized water, 190 µl ethanol and 60 µl Nafion (5 wt% solution in alcohol) were sonicated for 15 min in order to prepare inks. The aliquot of the ink necessary to reach a catalyst loading of 800 µg·cm^{-2} was pipetted on the glassy carbon disk (0.2475 cm^2). A carbon rod and a reversible hydrogen electrode (RHE) were used as counter and reference electrodes, respectively. An O_2-saturated aqueous solution 0.1 M $HClO_4$ was used as electrolyte. The disk potential was scanned between 0 and 1.1 V vs. RHE at 5 mV·s^{-1} while the ring potential was fixed at 1.2 V vs RHE. The collection efficiency of the RRDE electrode used was 0.37 ± 0.01.

Electrochemical characterization in PEMFC. PEMFC measurements were performed using an in-house fuel cell test bench with Biologic potentiostat and EC-Lab software. Catalysts inks were prepared by sonicating for 1 hour 20 mg of catalyst, 0.652 mL of 5 wt. % Nafion solution in lower aliphatic alcohols and 15 wt. % water, 0.327 mL 1-propanol, and 0.272 mL deionized water (18 MΩ). The catalyst ink was drop cast in 3 aliquots onto a 4.8 cm^2 Sigracet S10-BC gas diffusion layer giving a total loading of 4 mgcm^{-2} then dried at 70 °C for 1 hour. The cathode was hot pressed onto a Nafion 211 membrane with a Sigracet S28-BC anode containing 0.5 mgcm^{-2} Pt using a pressure of 2 tons and temperature of 135 °C for 2 minutes. The cell assembly consisted of a Fuel Cell Technologies Inc. single-cell with serpentine flow fields in graphite bipolar plates and gold-plated current collectors. PTFE sub-gaskets of 200 µm thickness were used at the cathode and anode giving a compression ratio of 30 %. The cell temperature was maintained at 80 °C operating at 100 % RH with pure O_2 and H_2 supplied to the cathode and anode at 200 sccm respectively at 2 bar absolute pressure. Polarization curves were recorded using linear sweep voltammetry at 1 mvs^{-1}. Stability tests were performed using chronoamperometry at 0.5 V for 15-18 hours.

DFT calculation and predictions. All ground state DFT calculations were performed at the GGA level with the Grid-based Projected Augmented Wave (GPAW) program[52, 53] and the Atomic Simulation Environment (ASE) package[54]. We used finite difference mode with the BEEF-vdW exchange and correlation functional[36], sampling the Brillouin zone with a 2 x 2 x 1 Monkhorst-Pack k-point set and a grid spacing of h = 0.18 Å. All structures were relaxed to a force below 0.05 eV / Å. The unit cell for all structure is periodic in x and y directions, while we applied a vacuum of 8 Å to each side of the catalyst plane along the z-axis. The data for the Me-N/C structures are adapted from our previous work[31], while the different Sn motifs are original models for this work. To evaluate the Gibbs free energy contribution, the entropy and

zero point energy corrections were added to the DFT energies[55]. We omitted any solvation correction on *OOH and *OH, as there is no widespread consensus in literature on how to treat the solvation on Me-N/C catalysts[56, 57]. Instead, we look at the computed activity trend within the series of metal, in order to eliminate most of the uncertainty related to the unknown interaction of the catalyst and the adsorbate with the surroundings. After publication, all structures with total energies will be available on Jan Rossmeisl' group homepage (http://nano.ku.dk/english/research/theoretical-electrocatalysis/katladb/).

Details about each experimental method is provided in the SI.

Data availability

The data supporting the findings of this study are available within this article and its Supplementary Information files, or from the corresponding author upon reasonable request. The Supplementary Information contains descriptions of methods of catalysts synthesis (SnNC, FeNC, CoNC, CuNC, NiNC and N-C), elemental analysis, BET-specific surface area and pore size distribution measurements, XRD, TEM, Aberration-corrected STEM, XANES and EXAFS, Mössbauer spectroscopy measurements, CO chemisorption, ORR stability tests, DFT calculation of quadrupole splitting value for SnN_x sites in ^{119}Sn Mössbauer spectra. The Supplementary Text discusses: the Sn-Sn back-scattering signal identified from EXAFS fitting; the reasons for lower site density in SnNC; DFT volcano plot methods on MNC. Supplementary Figures include: TEM image and XRD patterns (Figure S1); Mössbauer spectrum of FeNC (Figure S2); XAS at Fe $L_{3,2}$-edge and N_{1s} XPS spectrum for FeNC (Figure S3); STEM image of SnNC (Figure S4); K-edge XANES experimental spectra for SnNC (Figure S5); electrochemical characterization of FeNC, SnNC and CoNC (Figure S6); Stability results of SnNC (Figure S7); CO chemisorption and sites density of all MNC catalysts (Figure S8); Surface characterization of FeNC, SnNC, and N-C catalysts by N_2 physisorption (Figure S9); Polarization curves and selectively of MNC catalysts and NC (Figure S10); Pyrrolic structures volcano plot for M-N-C, where M=Fe, Sn, Co, Cu and Ni from DFT (Figure S11); Alternative fitting strategy for ^{119}Sn Mössbauer spectroscopy characterization (Figure S12); DFT-optimized structures (Figure S13 and S14); PEMFC polarization curves (Figure S15). It also includes Supplementary Tables 1-15.

References

51.   Jaouen F, Lefèvre M, Dodelet J-P, Cai M. Heat-Treated Fe/N/C Catalysts for O2 Electroreduction: Are Active Sites Hosted in Micropores? *The Journal of Physical Chemistry B* 2006, **110**(11)**:** 5553-5558.

52.   Hjorth Larsen A, Jorgen Mortensen J, Blomqvist J, Castelli IE, Christensen R, Dulak M*, et al.* The atomic simulation environment-a Python library for working with atoms. *J Phys Condens Matter* 2017, **29**(27)**:** 273002.

53.   Mortensen JJ, Hansen LB, Jacobsen KW. Real-space grid implementation of the projector augmented wave method. *Physical Review B* 2005, **71**(3)**:** 035109.

54.   Bahn SR, Jacobsen KW. An object-oriented scripting interface to a legacy electronic structure code. *Computing in Science & Engineering* 2002, **4**(3)**:** 56-66.

55.   Rossmeisl J, Qu ZW, Zhu H, Kroes GJ, Nørskov JK. Electrolysis of water on oxide surfaces. *Journal of Electroanalytical Chemistry* 2007, **607**(1)**:** 83-89.

56.   Calle-Vallejo F, Martínez JI, Rossmeisl J. Density functional studies of functionalized graphitic materials with late transition metals for oxygen reduction reactions. *Physical Chemistry Chemical Physics* 2011, **13**(34)**:** 15639-15643.

57.   Calle-Vallejo F, Krabbe A, Garcia-Lastra JM. How covalence breaks adsorption-energy scaling relations and solvation restores them. *Chem Sci* 2017, **8**(1)**:** 124-130.